



W₁₈O₄₉ nanowires-graphene nanocomposite for asymmetric supercapacitors employing AlCl₃ aqueous electrolyte

Mohammad R. Thalji^a, Gomaa A.M. Ali^b, Porun Liu^c, Yu Lin Zhong^c, Kwok Feng Chong^{a,*}

^a Faculty of Industrial Sciences & Technology, Universiti Malaysia Pahang, Gambang, 26300 Kuantan, Malaysia

^b Chemistry Department, Faculty of Science, Al-Azhar University, Assiut 71524, Egypt

^c Centre for Clean Environment and Energy, School of Environment and Science, Gold Coast Campus, Griffith University, Queensland 4222, Australia

ARTICLE INFO

Keywords:

Tungsten oxide
Graphene
Intercalation pseudocapacitance
Asymmetric supercapacitor
Energy density

ABSTRACT

W₁₈O₄₉ nanowires (NWs)-reduced graphene oxide (rGO) nanocomposite is examined as a new active material for supercapacitors electrode, which reveals its high specific capacitance and excellent rate performance in AlCl₃ aqueous electrolyte. Electrochemical studies show that the presence of rGO enhances Al³⁺ ions diffusion in the nanocomposite, thus provides more ions for intercalation pseudocapacitance. The fabrication of asymmetric supercapacitor W₁₈O₄₉ NWs-rGO//rGO demonstrates high specific capacitance of 365.5 F g⁻¹ at 1 A g⁻¹ and excellent cycling stability with 96.7% capacitance retention at 12,000 cycles. Interestingly, it delivers high energy density of 28.5 Wh kg⁻¹ and power density of 751 W kg⁻¹, which is the highest energy density value for all reported W₁₈O₄₉-based supercapacitor device. The work explores W₁₈O₄₉ NWs-rGO nanocomposite as a new electrode material for supercapacitors application with superior electrochemical performance, which may open up a new direction for high-performance energy storage in Al³⁺ electrolyte.

1. Introduction

The global modernization requires a substantial amount of energy supply, which can be fulfilled by renewable energy sources. In this context, energy storage system plays a vital role to ensure uninterrupted energy supply, especially for intermittent energy sources such as solar energy [1,2]. Among all energy storage systems, supercapacitors attain remarkable attention. The advancement of nanotechnology successfully engineers various nanomaterials for optimum charge storage in supercapacitors [3,4]. The charge storage in supercapacitors can be divided into electric double-layer capacitors (EDLC) and pseudocapacitors. EDLC involves the ions adsorption/desorption on the electrode surface where high-surface-area materials such as activated carbon (AC), carbon nanotubes (CNTs) or graphene are being popularly deployed [5]. On the other hand, pseudocapacitive materials such as MnO₂ and RuO_x store charge by fast and reversible redox reaction at the electrode surface and they usually show higher energy density than EDLC, however, at the cost of electrode stability [6,7]. Therefore, the quest for stable electrode materials to deliver high energy density is always desired. Recently, a new form of pseudocapacitance mechanism is proposed where the charge storage is achieved *via* intercalation of ions into the crystalline network. It is termed intercalation pseudocapacitance and it sheds light

to produce high energy density supercapacitors without compromising structural integrity. Only limited materials such as tungsten oxides and niobium oxides have been reported to exhibit intercalation pseudocapacitance [8–11].

Tungsten oxides (WO_x) are widely studied as electrode materials for supercapacitors application [9,12–16]. Among the WO_x, the monoclinic W₁₈O₄₉ nanostructure is regarded as a promising electrode material for the next-generation energy storage device, due to its abundance of oxygen-vacancies for electrical conductivity [17,18]. Most importantly, it possesses a unique crystal structure to render it as a suitable host material for ions intercalation process [19]. Nonetheless, the major issue in utilizing W₁₈O₄₉ as intercalation pseudocapacitor is the usage of acidic electrolyte as the source of intercalating H⁺ ions, which poses the corrosion problem for long term stability [20]. For these, Al³⁺ ion has been proposed as the substitute for intercalation ions to achieve remarkable electrochemical performance while remaining its long term stability [21–24]. The high charge-per-ion in Al³⁺ renders the supercapacitor to deliver high energy density while maintaining the safety and cost-effectiveness [25,26]. Nonetheless, the high charge density of Al³⁺ ion typically manifests strong electrostatic interaction with the host material lattice, which can cause slow Al³⁺ ion diffusion and decrease its electrochemical performance [27,28]. Therefore, a highly conductive

* Corresponding author.

E-mail address: ckfeng@ump.edu.my (K.F. Chong).

<https://doi.org/10.1016/j.cej.2020.128216>

Received 9 September 2020; Received in revised form 24 November 2020; Accepted 17 December 2020

Available online 24 December 2020

1385-8947/© 2020 Elsevier B.V. All rights reserved.

network is needed to facilitate Al^{3+} ions' mass transport [29].

Carbonaceous materials such as graphene, CNTs and AC [30–34] are commonly used to provide a conductive network for electrochemical enhancement. Graphene possesses a large surface area, high electrical conductivity and superior electrochemical stability, which makes it an ideal support material for nanocomposites [35,36]. As reported, graphene provides large platform for nanomaterials growth and enhances composites electrochemical performance by accelerating ions diffusion and charge transfer [37,38]. Another challenge regarding the electrochemical performance of $\text{W}_{18}\text{O}_{49}$ electrode is the limited potential window in aqueous electrolytes, which could limit the energy density [39–41]. Therefore, asymmetric supercapacitor (ASC) is often employed to enlarge device operating potential in the fabrication of energy storage system with high energy density.

Herein, we report a new active material $\text{W}_{18}\text{O}_{49}$ NWs-rGO for supercapacitor application. The nanocomposite is synthesized from precursors WCl_6 and graphene oxide (GO) by solvothermal method. The precursors mass ratio is investigated to generate optimum electrochemical performance. At optimum ratio, the $\text{W}_{18}\text{O}_{49}$ NWs-rGO nanocomposite shows high specific capacitance in Al^{3+} ion aqueous electrolyte with long term stability. It is discovered that Al^{3+} ions diffuse and intercalate into $\text{W}_{18}\text{O}_{49}$ crystal network to produce intercalation pseudocapacitance. The enhancement of charge storage in $\text{W}_{18}\text{O}_{49}$ NWs-rGO is due to the faster Al^{3+} ion diffusion in the presence of conductive rGO network. Finally, $\text{W}_{18}\text{O}_{49}$ NWs-rGO nanocomposite is used as the negative electrode in ASC device where high energy density of 28.5 Wh kg^{-1} and power density of 751 W kg^{-1} are achieved. This is the highest energy density achieved by $\text{W}_{18}\text{O}_{49}$ -based supercapacitor.

2. Experimental section

2.1. Materials synthesis

All the reagents were of analytical grade and used as received. GO was synthesized from the graphite flakes (+100 mesh, Graphene Supermarket) through the modified Hummers' method as previously reported by our group [42]. All $\text{W}_{18}\text{O}_{49}$ NWs-rGO nanocomposites were prepared through the solvothermal method. In brief, 0.351 g of WCl_6 powder ($\geq 99.9\%$, Sigma-Aldrich) with different GO mass were dispersed in 60 mL of absolute ethanol ($\geq 99.8\%$, Sigma-Aldrich) [21]. The mixture was sonicated for 15 min at room temperature. The homogeneous mixture was then transferred into a Teflon-lined autoclave and heated at 200°C for 10 h. After cooling down to room temperature, the $\text{W}_{18}\text{O}_{49}$ NWs-rGO nanocomposites were collected by centrifugation and washed with absolute ethanol for several times, followed by vacuum drying at 60°C overnight. Based on the above, a series of $\text{W}_{18}\text{O}_{49}$ NWs-rGO nanocomposites were synthesized by varying the mass ratio between WCl_6 and GO at 3:1, 4:1 and 5:1, in which they are labelled as W3G1, W4G1 and W5G1, respectively. The rGO sample was prepared as above procedure, but in the absence of WCl_6 . Similarly, the pure $\text{W}_{18}\text{O}_{49}$ sample was also prepared as above procedure in the absence of GO.

2.2. Materials characterizations

The morphologies of the materials were observed by Field emission scanning electron microscope (FESEM, JEOL JSM-7800F, USA) operating at 30.0 kV. X-ray diffraction (XRD) patterns were identified on X-ray diffractometer (Rigaku Miniflex II, Japan, $\text{Cu-K}\alpha$ radiation, $\lambda = 0.15418 \text{ nm}$) in the 2θ range from 5° to 80° . High-resolution transmission electron microscopy (HRTEM) images and selected area electron diffraction (SAED) patterns were obtained from a Philips Tecnai F20 (acceleration voltage of 200 kV) equipped with energy dispersive spectroscopy (EDS). X-ray photoelectron spectroscopy (XPS) analysis was carried out using PHI 5000 Versa Probe II with monochromatic $\text{Al-K}\alpha$ X-ray source at wide and narrow scan energy of 117.40 eV and 29.35 eV, respectively. Thermogravimetric analysis (TGA) was acquired using

a Hitachi STA7000 analyzer in an air atmosphere from room temperature to 700°C with a heating rate of $10^\circ\text{C min}^{-1}$. The Brunauer-Emmett-Teller (BET) surface area and the pore size distributions were performed by a micromeritics ASAP 2020 analyzer.

2.3. Electrochemical characterization

The working electrodes were prepared by mixing the samples (90 wt %), carbon black (5.0 wt%) and polyvinylidene difluoride (PVDF, 5.0 wt %) in N-methyl-2-pyrrolidinone (NMP), followed by pressing onto a piece of Ni foam and then dried at 70°C in a vacuum oven for 24 h. The electrochemical performance of electrodes was investigated at room temperature through a three-electrode configuration using a potentiostat-galvanostat Autolab (PGSTAT M101, Metrohm Autolab B.V.). The Ag/AgCl electrode and Pt mesh electrode were used as reference and counter electrodes, respectively. All electrochemical experiments were tested in 1 M AlCl_3 aqueous electrolyte. Cyclic voltammetry (CV), galvanostatic charge-discharge (GCD) and electrochemical impedance spectroscopy (EIS) techniques were conducted to characterize the electrochemical performance of the electrode materials. The long-term cycling stability was performed at a current density of 5 A g^{-1} for 12,000 GCD cycles.

2.4. Fabrication of ASC device

The ASC was assembled by utilizing $\text{W}_{18}\text{O}_{49}$ NWs-rGO nanocomposite as negative electrode and rGO sheets as positive electrode. A glass microfibre filter that was pre-soaked in 1 M AlCl_3 , used as a separator. The device assembly was conducted in an Ar-filled glovebox. To get higher charge storage performance for the ASC device, the optimum mass ratio of the two electrodes (m_+/m_-) is calculated to be ~ 3.12 which is balanced by considering the following Equation [43,44]:

$$\frac{m_+}{m_-} = \frac{C_{s-}\Delta V_-}{C_{s+}\Delta V_+} \quad (1)$$

where m is the mass of the active material (g), C_s is the specific capacitance (F g^{-1}) and ΔV is the potential window range (V) for positive and negative electrodes.

2.5. Calculation of supercapacitor performance

The specific capacitance (C_{sp} , F g^{-1}) in the three-electrode system was calculated from the GCD curves, using the following Equation [21,45]:

$$C_{sp} = \frac{I\Delta t}{m\Delta V} \quad (2)$$

where I is the applied current (A), Δt is the discharge time (s), m is the mass of the active material (g) and V is the discharge potential range (V).

The specific capacitance (C_{cell} , F g^{-1}) of the supercapacitor cell, energy density (E_D , Wh kg^{-1}) and power density (P_D , W kg^{-1}) were calculated from the GCD curves for the two-electrode configuration by following Equations [46,47]:

$$C_{cell} = \frac{4I\Delta t}{m\Delta V} \quad (3)$$

$$E_D = \frac{1}{8}C_{cell}\Delta V^2 \quad (4)$$

$$P_D = \frac{E_D}{\Delta t} \quad (5)$$

where m is the total mass for both positive and negative electrodes (g).

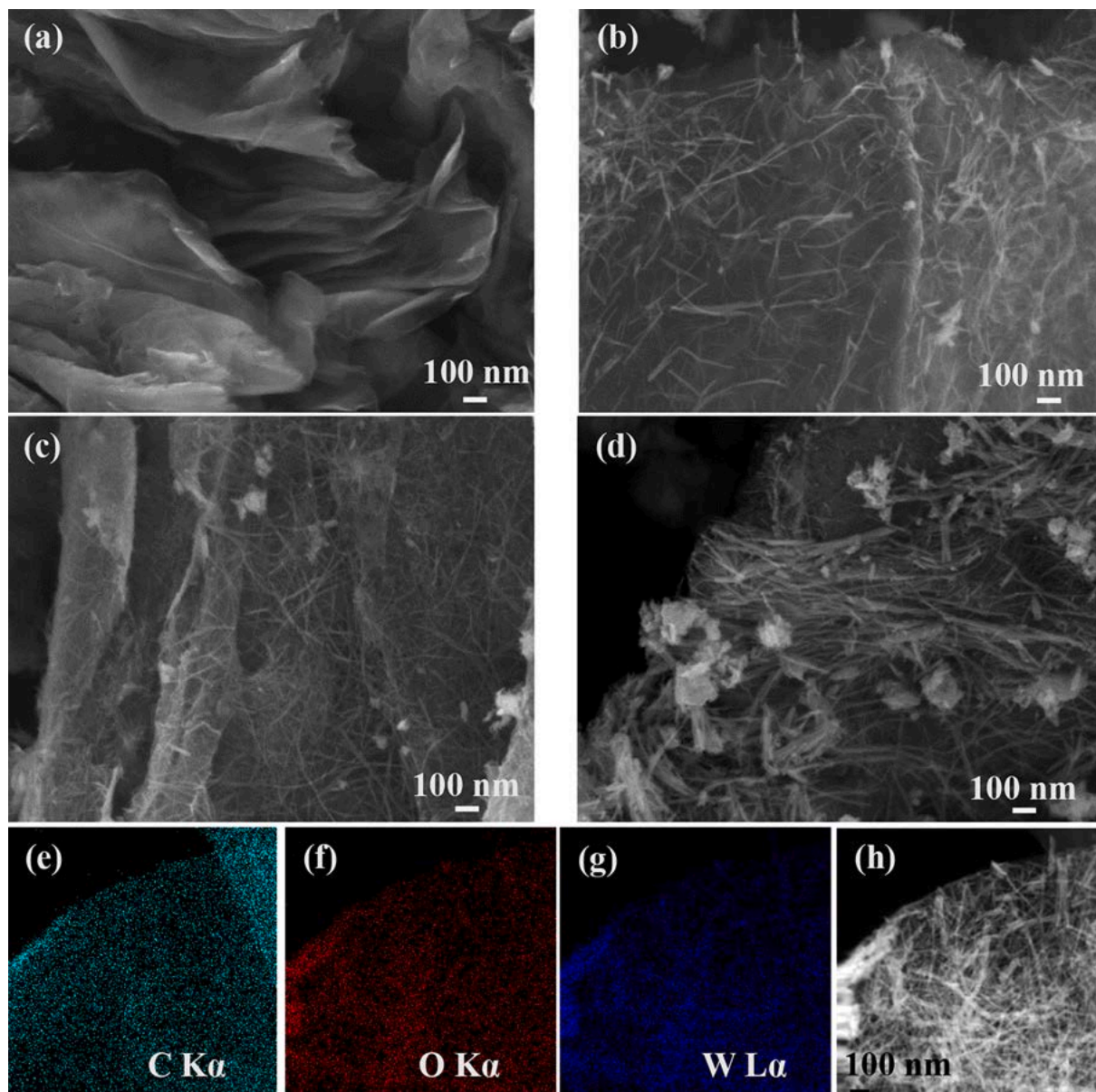


Fig. 1. FESEM images of (a) rGO sheets and W₁₈O₄₉ NWS-rGO nanocomposite at ratio (b) W3G1, (c) W4G1 and (d) W5G1. Elemental mapping images of (e) C, (f) O and (g) W elements for corresponding (h) W4G1 sample.

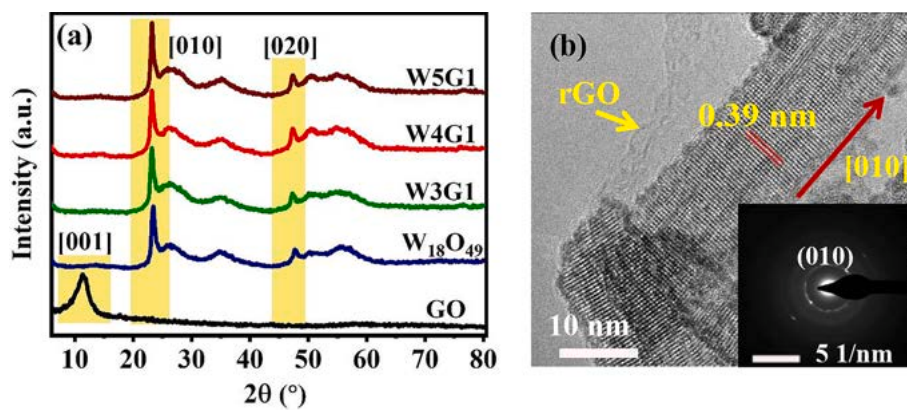


Fig. 2. (a) XRD patterns of the graphite oxide (GO), pure W₁₈O₄₉, and W₁₈O₄₉ NWS-rGO nanocomposites. (b) HRTEM image of the W4G1 nanocomposite, inset: SAED pattern of the nanocomposite.

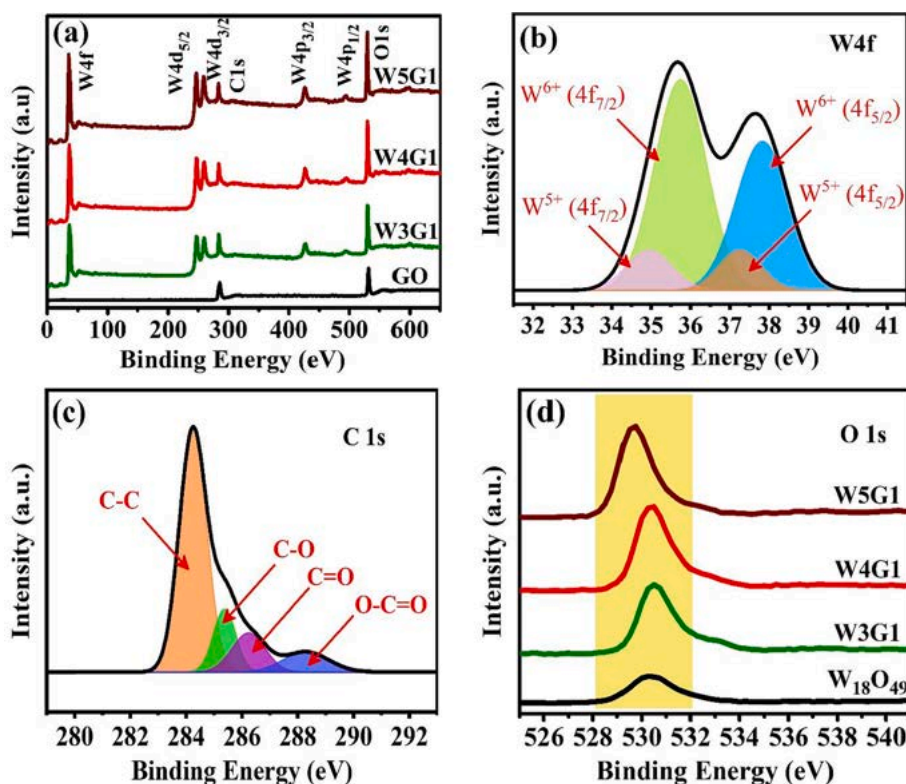


Fig. 3. (a) XPS survey spectra of GO and $W_{18}O_{49}$ NWs-rGO nanocomposites. High-resolution spectrum and corresponding deconvoluted spectra of W4G1 nanocomposite of the core-level (b) W4f and (c) C1s. (d) The O1s core-level spectra for $W_{18}O_{49}$ and $W_{18}O_{49}$ NWs-rGO nanocomposites.

3. Results and discussion

3.1. Structural characteristics

The formation of $W_{18}O_{49}$ NWs-rGO nanocomposite begins with electrostatic binding of W(VI) ions from WCl_6 onto the negatively-charged oxygen functional groups on GO sheets. At 200 °C solvothermal process, hydrolysis of W(VI) ions occurs to form $W_{18}O_{49}$ while GO is reduced to form rGO, leading to the formation of $W_{18}O_{49}$ -rGO nanocomposite. Different mass ratios of W(VI) and GO was used in this work to investigate the optimum ratio for energy storage application. It can be clearly seen that the reduced GO (rGO) exists as the fluffy sheets, upon solvothermal process (Fig. 1a). The addition of W(VI) leads to the formation of $W_{18}O_{49}$ in nanowires morphology, which are grown on the rGO sheets. By increasing W(VI) content from W3G1 to W5G1, more $W_{18}O_{49}$ NWs are grown on rGO sheets with higher aspect ratio (length to width). At low W(VI) content for W3G1 (Fig. 1b), the rGO sheets are not fully covered by $W_{18}O_{49}$ NWs where most of the area of rGO sheets are exposed. By increasing W(VI) at W4G1 sample (Fig. 1c), the $W_{18}O_{49}$ NWs coverage is increased to cover the entire rGO sheets, representing the structure with balanced ratio between $W_{18}O_{49}$ and rGO. Moreover, TEM image confirms that the $W_{18}O_{49}$ NWs are successfully formed and they cover the entire surface of the rGO sheets, as shown in Fig. S1a. However, at higher W(VI) for W5G1 sample (Fig. 1d), all the nanowires are obviously entangled and agglomerated on rGO sheets, an indication of excessive W(VI) which may shield the rGO effect in energy storage. Representative elemental mapping images (Fig. 1e-h) confirm the presence of W and O elements from $W_{18}O_{49}$ NWs on the rGO sheets (represented by C element mapping). Corresponding EDS spectrum is shown in Fig. S1b. In the absence of rGO sheets, $W_{18}O_{49}$ grows in the urchin-like morphology (Fig. S1c).

The presence of W and O elements in $W_{18}O_{49}$ NWs-rGO nanocomposite is confirmed as $W_{18}O_{49}$ crystal structure by XRD analysis (Fig. 2a), where the major diffraction peaks of $W_{18}O_{49}$ can be found in

Table 1

The XPS fitting results of W4f core-level for pure $W_{18}O_{49}$ and $W_{18}O_{49}$ NWs-rGO nanocomposites.

Material	Binding Energy (eV)			
	W^{5+}		W^{6+}	
	W4f _{7/2}	W4f _{5/2}	W4f _{7/2}	W4f _{5/2}
$W_{18}O_{49}$	34.70	36.87	35.35	37.47
W3G1	35.00	37.20	35.89	38.00
W4G1	34.91	37.10	35.70	37.80
W5G1	34.20	36.41	34.95	37.13

the nanocomposite at $2\theta = 23.2^\circ$ [010] and 47.3° [020]. They are also corresponding well to the monoclinic phase of $W_{18}O_{49}$ (P2/m, JCPDS card no.71–2450) [48]. The major plane of [010] can be clearly seen in HRTEM image of $W_{18}O_{49}$ NWs. They are ca. 12 nm in diameter with *d* spacing of 0.39 nm on the rGO sheet (Fig. 2b). On the other hand, the reduction of GO into rGO in the nanocomposite can be seen from the shifting of [001] peak of GO at $2\theta = 11.5^\circ$ to 26.0° , as the broad peak.

The detailed chemical states of as-prepared materials and their surface functional groups were further investigated by XPS. The survey spectrum (Fig. 3a) of GO reveals the presence of C and O elements. This indicates the successful oxidation process of graphite via modified Hummers' method. Moreover, the presence of a strong C1s peak in the $W_{18}O_{49}$ NWs-rGO nanocomposites confirms that the $W_{18}O_{49}$ NWs are successfully incorporated onto the rGO sheets during solvothermal process.

In W4f high-resolution XPS spectrum of W4G1 (Fig. 3b), the main spectrum can be deconvoluted into two pairs of peaks which refer to two different oxidation states of W element, namely W^{6+} and W^{5+} [18,49,50]. The peaks at binding energies of 35.70 and 37.80 eV can be assigned to W4f_{7/2} and W4f_{5/2} of W^{6+} , respectively. The second doublet peaks at binding energies of 34.91 and 37.10 eV correspond to the

Table 2Binding energies and percentages of GO and $W_{18}O_{49}$ NWs-rGO nanocomposites from the deconvoluted XPS spectra of C1s peaks.

Material	C—C		C—O		C=O		O—C=O	
	Binding Energy (eV)	Percentage (%)						
GO	283.9	41.4	285.9	28.5	287.2	24.9	289.3	5.2
W3G1	284.4	64.8	285.6	20.4	286.6	8.40	288.3	6.4
W4G1	284.2	65.0	285.4	13.5	286.2	12.6	288.3	8.9
W5G1	283.6	58.8	284.6	10.0	285.3	17.3	287.4	13.9

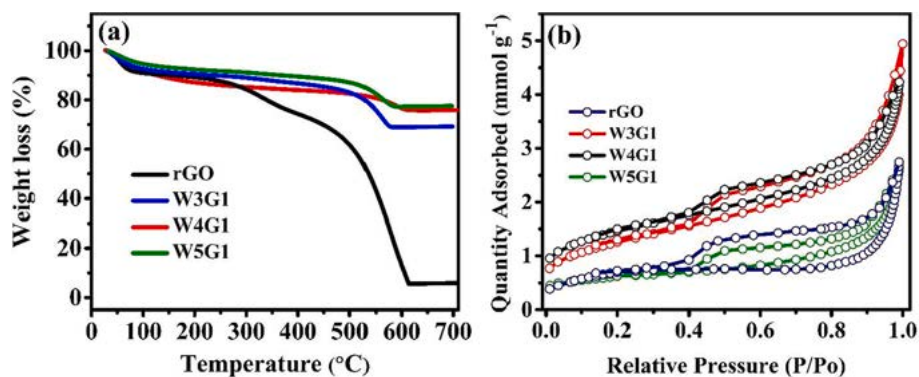


Fig. 4. (a) TGA analysis for rGO sheets and $W_{18}O_{49}$ NWs-rGO nanocomposites in air atmosphere at a heating rate of $10\text{ }^{\circ}\text{C min}^{-1}$. (b) The BET surface area calculated from N_2 adsorption/desorption isotherms of the rGO sheets and $W_{18}O_{49}$ NWs-rGO nanocomposites.

emission of $W4f_{7/2}$ and $W4f_{5/2}$ core levels from W^{5+} . Besides, $W4f$ core-level of the pure $W_{18}O_{49}$, W3G1 and W5G1 exhibit similar peaks as W4G1 nanocomposite spectrum with slight shift as shown in Fig. S2a-c and Table 1. It is worth noting that the position of $W4f$ peaks of the W3G1 and W4G1 nanocomposites shift to higher binding energy values as compared to that of the pure $W_{18}O_{49}$, which could be attributed to the interaction between $W_{18}O_{49}$ NWs and rGO sheets. For W5G1, the $W4f$ peaks are lower in binding energy as compared to that of pure $W_{18}O_{49}$, most probably due to the heavy stacking of NWs as seen in FESEM image.

The peak area ratios show that the percentages of W^{6+} and W^{5+} for W4G1 are 84.4% and 15.6%, respectively. Additionally, the oxygen vacancies in W3G1 (W^{5+}) is 16.7%, and in W5G1 (W^{5+}) is 14.2%. Conversely, the percentage of W^{5+} is 10.1% for the pure $W_{18}O_{49}$. This observation clearly shows the role of rGO in promoting more oxygen vacancies in $W_{18}O_{49}$ lattice. The oxygen vacancies may enhance charge storage performance, as proven in other study [51].

The core-level XPS spectrum of C1s for the W4G1 nanocomposite is shown in Fig. 3c. The major deconvoluted peak with binding energy of 284.2 eV is originated from the C—C bond of rGO. The residual oxygen can be seen from the deconvoluted peaks at 285.4, 286.3, and 288.3 eV, which can be assigned to the C—O, C=O, and O—C=O bonds, respectively [52]. The C1s core-level spectra for GO and other $W_{18}O_{49}$ NWs-rGO nanocomposites are shown as Fig. S2d-f and Table 2. The detailed measurements exhibit that the percentages of C—C bond for all nanocomposites significantly increase and the percentages of most oxygen-containing groups decrease. Meanwhile, The C/O atomic ratio of GO sheets is 0.71 and the corresponding values in the W3G1, W4G1, and W5G1 are 1.84, 1.86 and 1.43, respectively, which is similar to that obtained by the chemical reduction of GO method [53]. This clearly indicates the effective reduction of GO into rGO during solvothermal process. In the O1s core-level spectra (Fig. 3d), the pure $W_{18}O_{49}$ exhibits a broad peak with the binding energy of 530.2 eV, while the W3G1 and W4G1 nanocomposites peaks shift to high binding energy. This behavior strongly corroborates the formation of electronic interaction between $W_{18}O_{49}$ NWs and rGO sheets [54].

On the contrary, the O1s peak of W5G1 shows slight negative shift in

binding energy compared to that of pure $W_{18}O_{49}$. This negative shift indicates low electronic interaction between $W_{18}O_{49}$ NWs and rGO sheets in W5G1 as a result from higher percentage of C=O and O—C=O [55]. Additionally, this behavior indicates that the excess incorporation of $W_{18}O_{49}$ could adversely decrease the reduction degree of GO into rGO, which can be observed from Table 2. It is believed that the lower reduction degree of GO into rGO would pose a negative impact to W5G1 in the charge storage performance.

TGA in air atmosphere was used to determine the $W_{18}O_{49}$ content (wt.%) in all nanocomposite. As shown in Fig. 4a, the TGA curve of rGO sheets shows the vaporization of adsorbed water molecules (~ 10 wt%) at temperature below $100\text{ }^{\circ}\text{C}$, followed by the oxygen-functional groups removal (16 wt%) up to $400\text{ }^{\circ}\text{C}$. Beyond $400\text{ }^{\circ}\text{C}$, the huge mass loss (69 wt%) is observed up to $600\text{ }^{\circ}\text{C}$, which can be attributed to the decomposition and oxidation of carbon networks in rGO into CO_2 [56,57]. For $W_{18}O_{49}$ NWs-rGO nanocomposites, all TGA curves resemble thermal decomposition behavior of rGO, except at lower weight loss. The curves start with moisture vaporization (up to $100\text{ }^{\circ}\text{C}$), oxygen functional groups removal (up to $400\text{ }^{\circ}\text{C}$), oxidation of rGO into CO_2 (up to $600\text{ }^{\circ}\text{C}$) and stabilize at temperature higher than $600\text{ }^{\circ}\text{C}$. The $W_{18}O_{49}$ weight loading can be estimated from the balanced weight at temperature beyond $600\text{ }^{\circ}\text{C}$, by assuming insignificant weight loss for the phase transformation of $W_{18}O_{49}$ to WO_3 [58,59]. Hence, the $W_{18}O_{49}$ loadings in W3G1, W4G1 and W5G1 are estimated to be 63.3%, 69.9% and 71.6%, respectively. W4G1 exhibits more weight loss at temperature lower than $250\text{ }^{\circ}\text{C}$ which can be associated to the removal of surface-adsorbed water and structural water elimination. This may be related to its higher surface area, that will be discussed in the following section.

The N_2 sorption measurements for all as-prepared samples were carried out to characterize their BET surface area and porosity. Based on the adsorption/desorption curves shown in Fig. 4b, all samples exhibit type-IV isotherms. The solvothermal-reduced rGO possesses BET surface area of $53.0\text{ m}^2\text{ g}^{-1}$, and upon incorporation of $W_{18}O_{49}$, the surface area of W3G1 and W4G1 increase to $98.6\text{ m}^2\text{ g}^{-1}$ and $112\text{ m}^2\text{ g}^{-1}$, respectively. It shows the effective incorporation of $W_{18}O_{49}$ onto rGO sheets and simultaneously prevents stacking of the nanocomposites. On the other hand, the excessive $W_{18}O_{49}$ in W5G1 reduces its surface area to

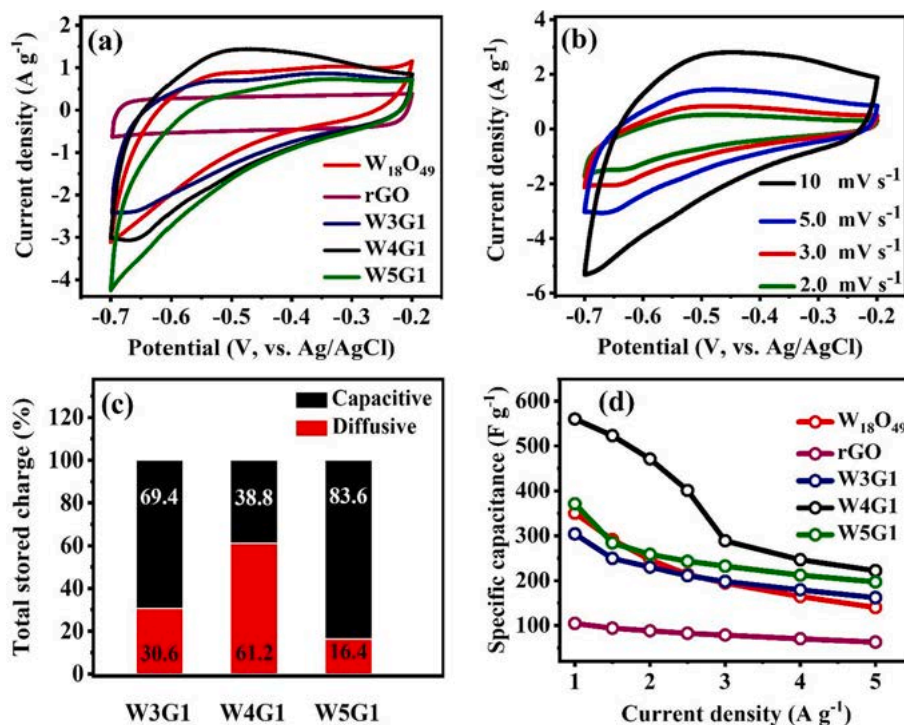
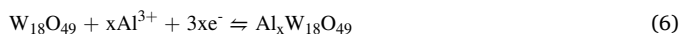


Fig. 5. (a) CV curves at the scan rate of 5 mV s⁻¹ for pure W₁₈O₄₉, rGO and W₁₈O₄₉ NWs-rGO nanocomposites electrodes. (b) CV curves at different scan rates for W4G1 electrode. (c) Capacitive and diffusive contributions of the W₁₈O₄₉ NWs-rGO nanocomposites electrodes to the charge storage. (d) The variation of specific capacitance (F g⁻¹) with different current densities (A g⁻¹) for all materials.

45.2 m² g⁻¹, consistent to the FESEM findings of heavy stacking of NWs. The Barrett-Joyner-Halenda (BJH) pore diameter calculation (Fig. S3) yields the pore size distribution of 4 nm, suggests the good mesoporosity for Al³⁺ penetration during charge-storage process.

3.2. Electrochemical properties

W₁₈O₄₉ nanostructure has been reported as an intercalation pseudocapacitive material in aqueous Al³⁺ ion electrolyte [21,23,24], where the reversible Al³⁺ intercalation/de-intercalation process is represented by the Equation:



To highlight the importance of W₁₈O₄₉ NWs incorporation onto the rGO sheets, all as-prepared materials were tested as the working electrodes in three-electrode system using 1 M AlCl₃ aqueous electrolyte (pH = 2.13). At this pH value, the Al³⁺ ion is in completely octahedral Al(H₂O)₆³⁺ form and the first dominant hydrolysis reaction is Al(H₂O)₆³⁺ ↔ Al(OH)(H₂O)₅²⁺ + H⁺ which becomes important at 3.0 < pH < 4.3 [60]. Moreover, the concentration of H⁺ ion is about 7.41 × 10⁻³ M, which is far smaller than the Al³⁺ ion concentration (1 M) used in this work. The dominant intercalation ion into W₁₈O₄₉ crystal lattice is Al³⁺ ion, instead of H⁺ ion. This is confirmed earlier through CV studies in our previous work (Fig. S4a) [21].

As shown in Fig. 5a, all W₁₈O₄₉ NWs-rGO nanocomposites electrodes exhibit rectangular-like CV curves from -0.7 to -0.2 V in 1 M AlCl₃ aqueous solution at a scan rate of 5 mV s⁻¹. Control experiment was also conducted on bare Ni foam to ensure the observed current density is originated from the samples (Fig. S4b). The charge storage properties can be briefly estimated from the area under the CV curve, where larger area represents higher charge storage. It can be clearly seen that the optimized sample W4G1 possesses highest charge storage performance than that of other samples, therefore it is selected for further electrochemical discussion. CV curves of W4G1 electrode at different scan rates (Fig. 5b) show the broad redox peaks between -0.5 and -0.7 V, where

they are more significant at lower scan rate (2.0 mV s⁻¹). These redox peaks can be ascribed to the reversible Al³⁺ ion intercalation/de-intercalation into W₁₈O₄₉ NWs-rGO structure [23,61], that contributes to the pseudocapacitive effect [10,62,63]. A similar phenomenon is also observed in W3G1 electrode with lower redox currents, while W5G1 electrode does not exhibit any redox peaks (Detailed CV curves for pure W₁₈O₄₉, rGO, W3G1 and W5G1 electrodes are shown in Fig. S5a-d). This is the first evidence of intercalation pseudocapacitive effect in W4G1 and W3G1, which could be related to the electronic interaction between W₁₈O₄₉ and rGO as shown in XPS analysis. The absence of redox peak in W5G1 is due to the excess content of W₁₈O₄₉ in W5G1 that causes lower reduction degree of GO into rGO. The low conductivity of GO impedes the Al³⁺ diffusion and therefore causes insignificant Al³⁺ ions intercalation. The addition of rGO is also proven to increase the rate capability of W₁₈O₄₉-rGO (W4G1, Fig. S5e), as observed in other studies [64,65].

CV results were extended to Trasatti's analysis for the investigation of charge storage mechanism in W₁₈O₄₉ NWs-rGO nanocomposites electrodes [21,63]. The total stored charge (Q_T), capacitive contributed charge (Q_C) and diffusive contributed charge (Q_D) were determined based on the Equation S1-S3 in the Supplementary Information. The Q_C can be obtained as intercept by extrapolating the plot of total measured voltammetric charge (Q_V) vs. v^{-1/2} from 2 to 300 mV s⁻¹ (Fig. S6a-c), and the Q_C values are computed to be 162.86, 198.10 and 158.71 C g⁻¹ for W3G1, W4G1 and W5G1, respectively. On the other hand, the Q_T values are obtained as intercept through extrapolation of the plot 1/Q_V vs. v^{1/2} as shown in Fig. S6d-f. It should be noted that the Q_T value of W4G1 is 510.20 C g⁻¹, which is higher than that of W3G1 (234.74 C g⁻¹) and W5G1 (189.75 C g⁻¹). The percentage of charge contribution from Q_C (capacitive) and Q_D (diffusive) for different samples are summarized as Fig. 5c. It can be seen that the dominant charge storage in W3G1 and W5G1 can be attributed to capacitive charge storage (69.4% for W3G1 and 83.6% for W5G1) where it depends on ions adsorption. Conversely, the dominant charge storage in W4G1 can be assigned to diffusive charge storage with 61.2% Q_D, suggests that the diffusion of Al³⁺ ions within W₁₈O₄₉ NWs-rGO contributes to the high specific capacitance

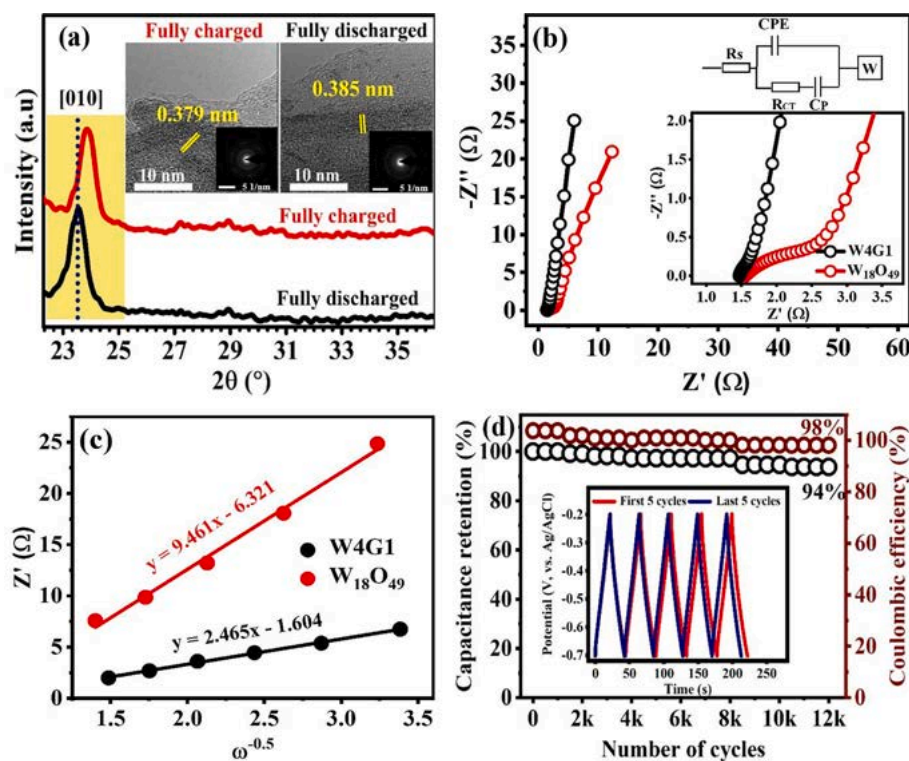


Fig. 6. (a) *Ex-situ* XRD patterns, *ex-situ* HRTEM and SAED images for the W4G1 electrode during fully charged/discharged process. (b) Nyquist plots for W4G1 and pure W₁₈O₄₉; the insets show the high-frequency region and equivalent circuit model. (c) The relationship curves between Z' and $\omega^{-0.5}$ in the low-frequency range of W₁₈O₄₉ and W4G1 electrodes. (d) Cycling stability and Coulombic efficiency of the W4G1 electrode at 5 A g⁻¹; the inset shows the GCD curves for the first 5 cycles and last 5 cycles.

[66,67]. This result proves that the optimized ratio between W₁₈O₄₉ and rGO (W4G1) renders higher electroactive surface area for the diffusion process. More Al³⁺ ions can diffuse and penetrate into the mesopores of W₁₈O₄₉, which produces more intercalation pseudocapacitance. On the other hand, the lower electroactive surface area of W3G1 and W5G1 limits the diffusion of Al³⁺ ions, thus making the ions adsorption as the main route for capacitive charge storage. Furthermore, the heavily entangled W₁₈O₄₉ NWs in W5G1 as seen in FESEM image also limit the Al³⁺ ions diffusion. A similar study reported that the diffusive charge storage increases at higher surface area, in which results in a significant enhancement of intercalation pseudocapacitance behavior [68,69].

Trasatti's analysis corroborates to the galvanostatic discharge (GD) results, as summarized in Fig. 5d. The dominant capacitive charge storage of W3G1 and W5G1 electrodes exhibit moderate increment in specific capacitance at lower current densities, a clear indication of double-layer capacitance. On the other hand, W4G1 electrode shows the substantial increment in specific capacitance when the current density decreases, which is associated with the longer diffusion time for Al³⁺ ions that contributes to higher charge storage. It can be seen that the highest specific capacitance is attained on W4G1 electrode with 560 F g⁻¹, followed by W5G1 (371 F g⁻¹), pure W₁₈O₄₉ (350 F g⁻¹), W3G1 (304 F g⁻¹) and rGO (104 F g⁻¹). The lower specific capacitance for W3G1 as compared to pure W₁₈O₄₉, can be explained by its higher rGO content that reduces the capacitance contribution from W₁₈O₄₉ NWs. The synergistic effect for fast Al³⁺ ion diffusion can be seen at optimized ratio of W4G1, to provide highest specific capacitance. Detailed GD curves are shown in Fig. S7a-f.

The charge storage of W4G1 electrode was further investigated by *ex-situ* XRD and HRTEM techniques, as shown in Fig. 6a. For the fully charged W4G1 electrode, the [010] peak shifts to higher diffraction angle, indicates the decrease in interlayer spacing, as confirmed by the HRTEM image to show the interlayer spacing d_{010} of 0.379 nm. During the charging process, the Al³⁺ intercalation forms the electrostatic interaction with the polar atoms in W₁₈O₄₉ structure that causes the d_{010} contraction. On the other hand, the fully discharged W4G1 electrode shows the d_{010} expansion to 0.385 nm as evidenced by the shifting of

[010] peak to lower diffraction angle and HRTEM image. This is due to the de-intercalation of Al³⁺ ions during the discharging process [70]. By combining these findings with the Trasatti's analysis, it can be deduced that the charge storage in W4G1 involves the diffusion of Al³⁺ ions within W₁₈O₄₉ NWs-rGO structure, followed by the intercalation/de-intercalation of Al³⁺ ions in the W₁₈O₄₉ crystal structure.

The role of rGO in W4G1 was further investigated by EIS, as shown in Fig. 6b. Prominently, W4G1 electrode exhibits lower charge transfer resistance (R_{CT}) as compared to that of pure W₁₈O₄₉ electrode, indicates higher conductivity and facile charge transfer during Al³⁺ ions intercalation [71,72], most probably associated to the addition of rGO in W4G1 (Detailed fitting circuit data as Table S1). The rGO role in enhancing Al³⁺ ions diffusion was studied by investigating the Al³⁺ ions diffusion coefficient ($D_{Al^{3+}}$) in W4G1 electrode and pure W₁₈O₄₉ electrode. The $D_{Al^{3+}}$ can be calculated from the following Equation [73,74]:

$$D_{Al^{3+}} = 0.5 \left(\frac{RT}{An^2 F^2 C \sigma_w} \right)^2 \quad (7)$$

where R is the gas constant (8.314 J mol⁻¹ K⁻¹), T is the absolute temperature (298.15 K), A is the surface area of the electrode (1 cm²), n is the number of electrons transferred, F is Faraday constant (96500 C mol⁻¹), C is the concentration of Al³⁺ ion in the solution (1 M), and σ_w is the Warburg coefficient, which is calculated by the following Equation (at low-frequency region):

$$Z' = R_s + R_{CT} + \sigma_w \omega^{-0.5} \quad (8)$$

where R_s is the electrolyte resistance, the σ_w can be obtained from the slope of linear fitting of the real part of impedance (Z') vs. the angular frequency ($\omega^{-0.5}$), as Fig. 6c. The $D_{Al^{3+}}$ of W4G1 electrode is computed to be 71.9×10^{-12} cm² s⁻¹, approximately 15 times higher than that of pure W₁₈O₄₉ electrode (4.89×10^{-12} cm² s⁻¹). The EIS data suggests that the incorporation rGO into W₁₈O₄₉ serves as a conductive platform to effectively accelerate Al³⁺ ions diffusion within the crystal structure, thus providing more Al³⁺ ions for intercalation pseudocapacitance. Furthermore, the electroactive surface area can be estimated (S_E , m²

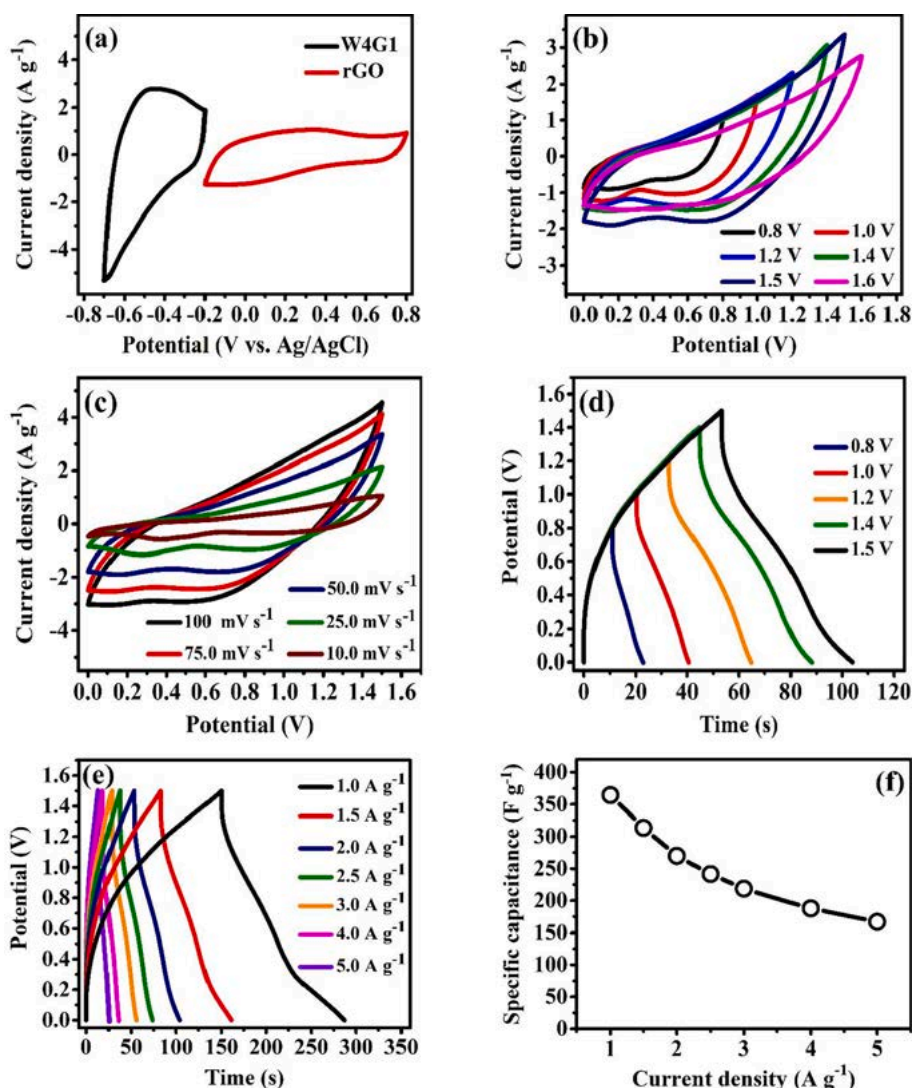


Fig. 7. (a) CV curves of the W4G1 and rGO electrodes at 10 mV s^{-1} . CV curves of the W4G1/rGO ASC device (b) at different operating potentials at 50 mV s^{-1} and (c) at different scan rates. GCD curves of the ASC device (d) at different operating potentials at 2 A g^{-1} and (e) at different current densities. (f) Specific capacitance of the ASC device at different current densities.

g^{-1}) from Equation $S_E = C_{dm}/C_d$ [21], where $C_{dm} = (2\pi f m Z^{-1})^{-1}$, Z' is the imaginary impedance from Nyquist plots at the frequency (10 mHz) and C_d is a constant value of $60 \mu\text{F cm}^{-2}$ and $40 \mu\text{F cm}^{-2}$ for metal oxide and nanocomposite electrode [75], respectively. The S_E value for W4G1 is $425.0 \text{ m}^2 \text{ g}^{-1}$, which is higher than those for pure $\text{W}_{18}\text{O}_{49}$ electrode ($166.2 \text{ m}^2 \text{ g}^{-1}$). It shows that the fast Al^{3+} ions diffusion and higher electroactive surface for W4G1 enhance its specific capacitance (560 F g^{-1}) as compared to pure $\text{W}_{18}\text{O}_{49}$ (350 F g^{-1}) electrode under similar discharge condition. Cycling stability of the W4G1 electrode was studied through continuous GCD tests up to 12,000 cycles at the current density of 5 A g^{-1} . Fig. 6d reveals the remarkable long-term cycling stability of W4G1 electrode with 94% retention of initial capacitance and around 98% Coulombic efficiency after 12,000 cycles, with insignificant change in the GCD curves.

3.3. Performance as asymmetric supercapacitor

$\text{W}_{18}\text{O}_{49}$ NWS-rGO//rGO ASC device was assembled in this work to expand the working potential in aqueous electrolyte. W4G1 was used as the negative electrode and rGO sheets was used as the positive electrode in 1 M AlCl_3 aqueous electrolyte. High voltage ASC can be obtained by combining the operating potential of W4G1 (from -0.7 to -0.2 V vs.

Ag/AgCl) and rGO (-0.2 to 0.8 V vs. Ag/AgCl) (Fig. 7a). The optimal mass ratio (m_+/m_-) was calculated at 3.12 for the balanced charge storage capacity between positive and negative electrodes. Fig. 7b shows the CV curves of the W4G1/rGO ASC device at different operating potential windows range from 0.8 to 1.6 V at the scan rate of 50 mV s^{-1} . At high operating potential window of 1.6 V , significant decrease of CV area is observed, which can be related to the electrode degradation. At 1.6 V , water decomposition occurs at negative electrode with H_2 evolution that increases the internal pressure of the cell and therefore deteriorates its electrochemical performance. Similar observation is reported in other works [76,77]. Therefore, the maximum operating potential window is determined to be 1.5 V . Fig. 7c shows the CV curves of the W4G1/rGO ASC device at different scan rates. At the cathodic scan, the reduction peak can be seen, and it is more prominent at lower scan rate. This could be attributed to the de-intercalation process occurs at the negative W4G1 electrode. Similar findings are observed at GCD results at 2 A g^{-1} (Fig. 7d) where the discharge curves exhibit the de-intercalation behavior. By increasing the ASC device working potential from 0.8 to 1.5 V , the specific capacitance of device improves from 121.3 to 269.9 F g^{-1} . The increment in specific capacitance and operating potential can improve the energy storage of ASC device. In addition, GCD measurements at different current densities retain their curve

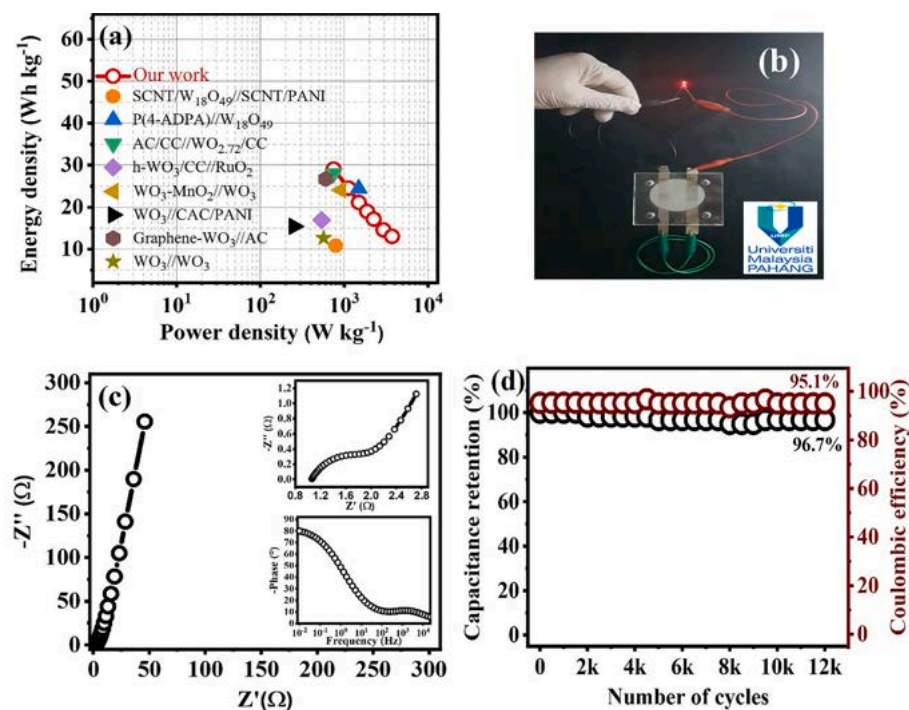


Fig. 8. (a) Ragone plot shows energy density and power density of the W4G1//rGO ASC in comparison to other ASCs in the literature. (b) The digital photograph of red color LED illuminated by two ASCs connected in series. (c) Nyquist plot of the W4G1//rGO ASC; the insets show the intercept in the high frequency region and Bode plot. (d) Cycling stability and Coulombic efficiency of the W4G1//rGO ASC device. (For interpretation of the references to color in this figure legend, the reader is referred to the web version of this article.)

shape, an indication of device high reversibility (Fig. 7e). The summary of specific capacitance values are depicted as Fig. 7f, with the highest specific capacitance of 365.53 F g^{-1} at 1 A g^{-1} .

The specific capacitance results are translated into Ragone plot in Fig. 8a, to show the device energy density and power density. It can be seen that the W4G1//rGO device produces energy from 13.0 to 28.5 Wh kg^{-1} , which corresponds to 3744 and 751 W kg^{-1} power density, respectively. To the best of our knowledge, this is the highest energy density produced by $\text{W}_{18}\text{O}_{49}$ -based supercapacitor [24,46,78] and its performance is also competitive to other WO_x -based supercapacitors [79–83] as shown in Table S2. The high energy density of W4G1//rGO ASC device is also manifested by Fig. 8b where a red LED light was powered up for up to 7 min by connecting it to two W4G1//rGO ASC device in series.

EIS was employed to further confirm the ASC performance (Fig. 8c). The Nyquist plot of the W4G1//rGO ASC device was measured in the frequency range from 0.01 Hz to 100 kHz at open circuit potential. After fitting EIS data (circuit fitting as Fig. S8b), low R_S (1.06Ω) and R_{CT} (0.845Ω) values are achieved, indicates the high electrical conductivity of the device. Moreover, in the Bode plot, characteristic frequency (f^*) at the phase angle of -45° of the W4G1//rGO ASC device is determined to be 1.38 Hz , corresponds to the relaxation time (τ) [84], ($\tau = 1/f^*$), of 0.72 s . The small τ value of ASC device indicates the fast frequency response, again confirms the high rate capability [85,86]. The phase angle at low frequency is found to be at -80° , very close to the -90° by the ideal supercapacitor device [87]. Another interesting point is that the ASC device possesses long-term cycling stability at a constant current density of 5 A g^{-1} , as shown in Fig. 8d. It manifests superior cycling stability of 96.7% retention of the initial capacitance as well as high Coulombic efficiency (95.1%) after $12,000$ cycles. All these alluring results make our ASC to be the promising device for high-performance energy storage systems.

4. Conclusions

For the first time, the $\text{W}_{18}\text{O}_{49}$ NWs-rGO nanocomposite is reported as an electrode for supercapacitors application. The rGO sheets provide a conductive platform for $\text{W}_{18}\text{O}_{49}$ NWs growth and promote the formation

of more oxygen vacancies in $\text{W}_{18}\text{O}_{49}$ NWs, thus enhances the diffusion of Al^{3+} ions within the structure and increases the intercalation pseudocapacitance. The electroactive surface area is also enhanced by the addition of rGO sheets in $\text{W}_{18}\text{O}_{49}$ NWs-rGO nanocomposite. The assembled ASC device with $\text{W}_{18}\text{O}_{49}$ NWs-rGO nanocomposite as negative electrode and rGO as positive electrode, delivers high energy density of 28.5 Wh kg^{-1} and power density of 751 W kg^{-1} , suggesting the promising potential of $\text{W}_{18}\text{O}_{49}$ NWs-rGO nanocomposite for high-performance supercapacitors application.

Declaration of Competing Interest

The authors declare that they have no known competing financial interests or personal relationships that could have appeared to influence the work reported in this paper.

Acknowledgments

The authors would like to acknowledge the funding from the Ministry of Education Malaysia in the form of [RDU1901186: FRGS/1/2019/STG07/UMP/02/6] and Malaysia Toray Science Foundation grant RDU201502.

Appendix A. Supplementary data

Supplementary data to this article can be found online at <https://doi.org/10.1016/j.cej.2020.128216>.

References

- [1] T.M. Gür, Review of electrical energy storage technologies, materials and systems: challenges and prospects for large-scale grid storage, *Energy Environ. Sci.* 11 (2018) 2696–2767, <https://doi.org/10.1039/C8EE01419A>.
- [2] D. Di Lecce, R. Verrelli, J. Hassoun, Lithium-ion batteries for sustainable energy storage: recent advances towards new cell configurations, *Green Chem.* 19 (2017) 3442–3467, <https://doi.org/10.1039/C7GC01328K>.
- [3] J. Zhou, M. Guo, L. Wang, Y. Ding, Z. Zhang, Y. Tang, C. Liu, S. Luo, 1T-MoS₂ nanosheets confined among TiO₂ nanotube arrays for high performance supercapacitor, *Chem. Eng. J.* 366 (2019) 163–171, <https://doi.org/10.1016/j.cej.2019.02.079>.

- [4] W.-J. Zhang, K.-J. Huang, A review of recent progress in molybdenum disulfide-based supercapacitors and batteries, *Inorg. Chem. Front.* 4 (2017) 1602–1620, <https://doi.org/10.1039/C7QI00515F>.
- [5] C. Schütter, S. Pohlmann, A. Balducci, Industrial requirements of materials for electrical double layer capacitors: impact on current and future applications, *Adv. Energy Mater.* 9 (2019) 1900334, <https://doi.org/10.1002/aenm.201900334>.
- [6] J.B. Cook, T.C. Lin, H.S. Kim, A. Siorodia, B.S. Dunn, S.H. Tolbert, Suppression of electrochemically driven phase transitions in nanostructured MoS₂ pseudocapacitors probed using operando x-ray diffraction, *ACS Nano* 13 (2019) 1223–1231, <https://doi.org/10.1021/acsnano.8b06381>.
- [7] X. Sun, T. Xu, J. Bai, C. Li, MnO₂ nanosheets grown on multichannel carbon nanofibers containing amorphous cobalt oxide as a flexible electrode for supercapacitors, *ACS Appl. Energy Mater.* 2 (2019) 8675–8684, <https://doi.org/10.1021/acsaem.9b01650>.
- [8] J.B. Mitchell, N.R. Geise, A.R. Paterson, N.C. Osti, Y. Sun, S. Fleischmann, R. Zhang, L.A. Madsen, M.F. Toney, D.-E. Jiang, A.I. Kolesnikov, E. Mamontov, V. Augustyn, Confined interlayer water promotes structural stability for high-rate electrochemical proton intercalation in tungsten oxide hydrates, *ACS Energy Lett.* 4 (2019) 2805–2812, <https://doi.org/10.1021/acsenerylett.9b02040.s001>.
- [9] M. Zhu, W. Meng, Y. Huang, Y. Huang, C. Zhi, Proton-insertion-enhanced pseudocapacitance based on the assembly structure of tungsten oxide, *ACS Appl. Mater. Interfaces* 6 (2014) 18901–18910, <https://doi.org/10.1021/am504756u>.
- [10] V. Augustyn, J. Come, M.A. Lowe, J.W. Kim, P.-L. Taberna, S.H. Tolbert, H. D. Abruna, P. Simon, B. Dunn, High-rate electrochemical energy storage through Li⁺ intercalation pseudocapacitance, *Nat. Mater.* 12 (2013) 518–522, <https://doi.org/10.1038/nmat3601>.
- [11] L. Kong, X. Cao, J. Wang, W. Qiao, L. Ling, D. Long, Revisiting Li⁺ intercalation into various crystalline phases of Nb₂O₅ anchored on graphene sheets as pseudocapacitive electrodes, *J. Power Sources* 309 (2016) 42–49, <https://doi.org/10.1016/j.jpowsour.2016.01.087>.
- [12] S. Yoon, E. Kang, J.K. Kim, C.W. Lee, J. Lee, Development of high-performance supercapacitor electrodes using novel ordered mesoporous tungsten oxide materials with high electrical conductivity, *Chem. Commun.* 47 (2011) 1021–1023, <https://doi.org/10.1039/C0CC03594G>.
- [13] D. Mandal, P. Routh, A.K. Nandi, A new facile synthesis of tungsten oxide from tungsten disulfide: structure dependent supercapacitor and negative differential resistance properties, *Small* 14 (2018) 1702881, <https://doi.org/10.1002/sml.201702881>.
- [14] X. Wu, S. Yao, Flexible electrode materials based on WO₃ nanotube bundles for high performance energy storage devices, *Nano Energy* 42 (2017) 143–150, <https://doi.org/10.1016/j.nanoen.2017.10.058>.
- [15] M. Yang, L. Li, L.i. Ma, B. Wei, C. Yao, J. Li, Macroporous defective tungsten oxide nanostructure electrodes deliver ultrahigh capacitance and remarkable long cyclic durability in LiCl electrolyte, *Ceram. Int.* 44 (2018) 22718–22724, <https://doi.org/10.1016/j.ceramint.2018.09.054>.
- [16] F. Zheng, C. Xi, J. Xu, Y.i. Yu, W. Yang, P. Hu, Y. Li, Q. Zhen, S. Bashir, J.L. Liu, Facile preparation of WO₃ nano-fibers with super large aspect ratio for high performance supercapacitor, *J. Alloy. Compd.* 772 (2019) 933–942, <https://doi.org/10.1016/j.jallcom.2018.09.085>.
- [17] A.W. Bayeh, D.M. Kabtamu, Y.-C. Chang, G.-C. Chen, H.-Y. Chen, T.-R. Liu, T. H. Wondimu, K.-C. Wang, C.-H. Wang, Hydrogen-treated defect-rich W₁₈O₄₉ nanowire-Modified graphite felt as high-performance electrode for vanadium redox flow battery, *ACS Appl. Energy Mater.* 2 (2019) 2541–2551, <https://doi.org/10.1021/acsaem.8b02158>.
- [18] X. Zhong, Y. Sun, X. Chen, G. Zhuang, X. Li, J.G. Wang, Mo doping induced more active sites in urchin-like W₁₈O₄₉ nanostructure with remarkably enhanced performance for hydrogen evolution reaction, *Adv. Funct. Mater.* 26 (2016) 5778–5786, <https://doi.org/10.1002/adfm.201601732>.
- [19] S. Cong, F. Geng, Z. Zhao, Tungsten oxide materials for optoelectronic applications, *Adv. Mater.* 28 (2016) 10518–10528, <https://doi.org/10.1002/adma.201601109>.
- [20] J. Jung, D.H. Kim, W₁₈O₄₉ nanowires assembled on carbon felt for application to supercapacitors, *Appl. Surf. Sci.* 433 (2018) 750–755, <https://doi.org/10.1016/j.apsusc.2017.10.109>.
- [21] M.R. Thalji, G.A.M. Ali, H. Algarni, K.F. Chong, Al³⁺ ion intercalation pseudocapacitance study of W₁₈O₄₉ nanostructure, *J. Power Sources* 438 (2019) 227028, <https://doi.org/10.1016/j.jpowsour.2019.227028>.
- [22] S.J. Yoo, J.W. Lim, Y.-E. Sung, Y.H. Jung, H.G. Choi, D.K. Kim, Fast switchable electrochromic properties of tungsten oxide nanowire bundles, *Appl. Phys. Lett.* 90 (2007) 173126, <https://doi.org/10.1063/1.2734395>.
- [23] Y. Tian, W. Zhang, S. Cong, Y. Zheng, F. Geng, Z. Zhao, Unconventional aluminum ion intercalation/deintercalation for fast switching and highly stable electrochromism, *Adv. Funct. Mater.* 25 (2015) 5833–5839, <https://doi.org/10.1002/adfm.201502638>.
- [24] K. Li, Y. Shao, S. Liu, Q. Zhang, H. Wang, Y. Li, R.B. Kaner, Aluminum-ion-intercalation supercapacitors with ultrahigh areal capacitance and highly enhanced cycling stability: power supply for flexible electrochromic devices, *Small* 13 (2017) 1700380, <https://doi.org/10.1002/sml.201700380>.
- [25] Y. Hu, B. Luo, D. Ye, X. Zhu, M. Lyu, L. Wang, An innovative freeze-dried reduced graphene oxide supported SnS₂ cathode active material for aluminum-ion batteries, *Adv. Mater.* 29 (2017) 1–6, <https://doi.org/10.1002/adma.201606132>.
- [26] Y. Hu, D. Sun, B. Luo, L. Wang, Recent progress and future trends of aluminum batteries, *Energy Technol.* 7 (2019) 86–106, <https://doi.org/10.1002/ente.201800550>.
- [27] S.K. Das, S. Mahapatra, H. Lahan, Aluminium-ion batteries: developments and challenges, *J. Mater. Chem. A* 5 (2017) 6347–6367, <https://doi.org/10.1039/C7TA00228A>.
- [28] R.K. Guduru, J.C. Icaza, A brief review on multivalent intercalation batteries with aqueous electrolytes, *Nanomaterials* 6 (2016) 1–19, <https://doi.org/10.3390/nano6030041>.
- [29] H. Lahan, R. Boruah, A. Hazarika, S.K. Das, Anatase TiO₂ as an anode material for rechargeable aqueous aluminum-ion batteries: remarkable graphene induced aluminum ion storage phenomenon, *J. Phys. Chem. C* 121 (2017) 26241–26249, <https://doi.org/10.1021/acs.jpcc.7b09494>.
- [30] Z. Chen, V. Augustyn, J. Wen, Y. Zhang, M. Shen, B. Dunn, Y. Lu, High-performance supercapacitors based on intertwined CNT/V₂O₅ nanowire nanocomposites, *Adv. Mater.* 23 (2011) 791–795, <https://doi.org/10.1002/adma.201003658>.
- [31] Y. Lu, Z. Zhang, X. Liu, W. Wang, T. Peng, P. Guo, H. Sun, H. Yan, Y. Luo, NiCo₂S₄/carbon nanotube nanocomposites with a chain-like architecture for enhanced supercapacitor performance, *CrystEngComm* 18 (2016) 7696–7706, <https://doi.org/10.1039/c6ce01556e>.
- [32] G.A.M. Ali, M.R. Thalji, W.C. Soh, H. Algarni, K.F. Chong, One-step electrochemical synthesis of MoS₂/graphene composite for supercapacitor application, *J. Solid State Electrochem.* 24 (2020) 25–34, <https://doi.org/10.1007/s10008-019-04449-5>.
- [33] D. Deng, B.S. Kim, M. Gopiraman, I.S. Kim, Needle-like MnO₂/activated carbon nanocomposites derived from human hair as versatile electrode materials for supercapacitors, *RSC Adv.* 5 (2015) 81492–81498, <https://doi.org/10.1039/c5ra16624a>.
- [34] K. Singh, S. Kumar, K. Agarwal, K. Soni, V. Ramana Gedela, K. Ghosh, Three-dimensional graphene with MoS₂ nano-hybrid as potential energy storage/transfer device, *Sci. Rep.* 7 (2017) 1–12, <https://doi.org/10.1038/s41598-017-09266-2>.
- [35] Y. Sun, Q. Wu, G. Shi, Graphene based new energy materials, *Energy Environ. Sci.* 4 (2011) 1113, <https://doi.org/10.1039/c0ee00683a>.
- [36] H. Sun, J. Zhu, D. Baumann, L. Peng, Y. Xu, I. Shakir, Y.u. Huang, X. Duan, Hierarchical 3D electrodes for electrochemical energy storage, *Nat. Rev. Mater.* 4 (2019) 45–60, <https://doi.org/10.1038/s41578-018-0069-9>.
- [37] C. Zhang, N. Ping, L. Shen, H. Li, G. Pang, X. Zhang, Li₃V₂(PO₄)₃/nitrogen-doped reduced graphene oxide nanocomposite with enhanced lithium storage properties, *J. Solid State Electrochem.* 20 (2016) 1983–1990, <https://doi.org/10.1007/s10008-016-3204-9>.
- [38] J. Azadmanjiri, V.K. Srivastava, P. Kumar, J. Wang, A. Yu, Graphene-supported 2D transition metal oxide heterostructures, *J. Mater. Chem. A* 6 (2018) 13509–13537, <https://doi.org/10.1039/C8TA03404D>.
- [39] Y. Tian, S. Cong, W. Su, H. Chen, Q. Li, F. Geng, Z. Zhao, Synergy of W₁₈O₄₉ and polyaniline for smart supercapacitor electrode integrated with energy level indicating functionality, *Nano Lett.* 14 (2014) 2150–2156, <https://doi.org/10.1021/nl5004448>.
- [40] S. Park, H.-W. Shim, C.W. Lee, H.J. Song, J.-C. Kim, D.-W. Kim, High-power and long-life supercapacitive performance of hierarchical, 3-D urchin-like W₁₈O₄₉ nanostructure electrodes, *Nano Res.* 9 (2016) 633–643, <https://doi.org/10.1007/s12274-015-0943-3>.
- [41] T. Meng, Z. Kou, I.S. Aminu, X. Hong, Q. Li, Y. Tang, Y. Zhao, S. Liu, L. Mai, S. Mu, Electronic structure control of tungsten oxide activated by Ni for ultrahigh-performance supercapacitors, *Small* 14 (2018) 1–8, <https://doi.org/10.1002/sml.201800381>.
- [42] S.P. Lee, G.A.M. Ali, H. Algarni, K.F. Chong, Flake size-dependent adsorption of graphene oxide aerogel, *J. Mol. Liq.* 277 (2019) 175–180, <https://doi.org/10.1016/j.molliq.2018.12.097>.
- [43] Z.-B. Zhai, K.-J. Huang, X.u. Wu, Superior mixed Co-Cd selenide nanorods for high performance alkaline battery-supercapacitor hybrid energy storage, *Nano Energy* 47 (2018) 89–95, <https://doi.org/10.1016/j.nanoen.2018.02.059>.
- [44] Z.-B. Zhai, K.-J. Huang, X.u. Wu, H. Hu, Y. Xu, R.-M. Chai, Metal-organic framework derived small sized metal sulfide nanoparticles anchored on N-doped carbon plates for high-capacity energy storage, *Dalton Trans.* 48 (2019) 4712–4718, <https://doi.org/10.1039/C9DT00195F>.
- [45] M.R. Thalji, G.A.M. Ali, S. Poh, K.F. Chong, Solvothermal synthesis of reduced graphene oxide as electrode material for supercapacitor application, *Chem. Adv. Mater.* 4 (2019) 17–26.
- [46] H. Peng, R. Zhao, J. Liang, S. Wang, F. Wang, J. Zhou, G. Ma, Z. Lei, Template-confined growth of poly(4-aminodiphenylamine) nanosheets as positive electrode toward superlong-life asymmetric supercapacitor, *ACS Appl. Mater. Interfaces* 10 (43) (2018) 37125–37134, <https://doi.org/10.1021/acsaami.8b14138.s001>.
- [47] H. Peng, G. Ma, K. Sun, Z. Zhang, J. Li, X. Zhou, Z. Lei, A novel aqueous asymmetric supercapacitor based on petal-like cobalt selenide nanosheets and nitrogen-doped porous carbon networks electrodes, *J. Power Sources* 297 (2015) 351–358, <https://doi.org/10.1016/j.jpowsour.2015.08.025>.
- [48] Y. Wang, H. Huang, S. Duan, X. Liu, J. Sun, T. Hayat, A. Alsaedi, J. Li, A new application of a mesoporous hybrid of tungsten oxide and carbon as an adsorbent for elimination of Sr²⁺ and Co²⁺ from an aquatic environment, *ACS Sustain. Chem. Eng.* 6 (2018) 2462–2473, <https://doi.org/10.1021/acssuschemeng.7b03818>.
- [49] T. Paik, M. Cargnello, T.R. Gordon, S. Zhang, H. Yun, J.D. Lee, H.Y. Woo, S.J. Oh, C.R. Kagan, P. Fornasiero, C.B. Murray, Photocatalytic hydrogen evolution from substoichiometric colloidal WO_{3-x} nanowires, *ACS Energy Lett.* 3 (2018) 1904–1910, <https://doi.org/10.1021/acsenerylett.8b00925>.
- [50] D.R. Jones, V. Gomez, J.C. Bear, B. Rome, F. Mazzali, J.D. McGettrick, A.R. Lewis, S. Margadonna, W.A. Al-Masry, C.W. Dunnill, Active removal of waste dye pollutants using Ta₃N₅/W₁₈O₄₉ nanocomposite fibres, *Sci. Rep.* 7 (2017) 1–16, <https://doi.org/10.1038/s41598-017-04240-4>.
- [51] S. Liu, Y. Yin, D. Ni, K.S. Hui, M. Ma, S. Park, K.N. Hui, C.-Y. Ouyang, S.C. Jun, New insight into the effect of fluorine doping and oxygen vacancies on electrochemical performance of Co₂MnO₄ for flexible quasi-solid-state asymmetric supercapacitors,

- Energy Storage Mater. 22 (2019) 384–396, <https://doi.org/10.1016/j.ensm.2019.02.014>.
- [52] B. Ma, E. Huang, G. Wu, W. Dai, N. Guan, L. Li, Fabrication of WO_{2.72}/RGO nanocomposites for enhanced photocatalysis, RSC Adv 7 (2017) 2606–2614, <https://doi.org/10.1039/c6ra26416f>.
- [53] S. Mao, K. Yu, S. Cui, Z. Bo, G. Lu, J. Chen, A new reducing agent to prepare single-layer, high-quality reduced graphene oxide for device applications, Nanoscale 3 (2011) 2849, <https://doi.org/10.1039/c1nr10270b>.
- [54] S. Sui, Y. Liao, Y. Xie, X. Wang, L. Li, Z. Luo, W. Zhou, G. Wang, K. Pan, A. Cabot, High catalytic activity of W₁₈O₄₉ nanowire-reduced graphite oxide composite counter electrode for dye-sensitized solar cells, ChemistrySelect 2 (2017) 8927–8935, <https://doi.org/10.1002/slct.201701436>.
- [55] H. Kalil, S. Maher, T. Bose, M. Bayachou, Manganese oxide/hemin-functionalized graphene as a platform for peroxydinitrate sensing, J. Electrochem. Soc. 165 (2018) G3133–G3140, <https://doi.org/10.1149/2.0221812jes>.
- [56] R. Kumar, R. Matsuo, K. Kishida, M.M. Abdel-Galeil, Y. Suda, A. Matsuda, Homogeneous reduced graphene oxide supported NiO-MnO₂ ternary hybrids for electrode material with improved capacitive performance, Electrochim. Acta 303 (2019) 246–256, <https://doi.org/10.1016/j.electacta.2019.02.084>.
- [57] C. Chen, J. Xi, Y. Han, L. Peng, W. Gao, Z. Xu, C. Gao, Ultralight graphene microporocorns for multifunctional composite applications, Carbon 139 (2018) 545–555, <https://doi.org/10.1016/j.carbon.2018.07.020>.
- [58] X. Li, S. Yang, J. Sun, P. He, X. Xu, G. Ding, Tungsten oxide nanowire-reduced graphene oxide aerogel for high-efficiency visible light photocatalysis, Carbon 78 (2014) 38–48, <https://doi.org/10.1016/j.carbon.2014.06.034>.
- [59] S. Sun, Y. Zhao, Y. Xia, Z. Zou, G. Min, Y. Zhu, Bundled tungsten oxide nanowires under thermal processing, Nanotechnology 19 (2008) 305709, <https://doi.org/10.1088/0957-4484/19/30/305709>.
- [60] T.W. Swaddle, J. Rosenqvist, P. Yu, E. Bylaska, B.L. Phillips, W.H. Casey, Kinetic evidence for five-coordination in AlOH₂⁺ ion, Science 308 (2005) 1450–1453, <https://doi.org/10.1126/science.1110231>.
- [61] J.W. Kim, V. Augustyn, B. Dunn, The effect of crystallinity on the rapid pseudocapacitive response of Nb₂O₅, Adv. Energy Mater. 2 (2012) 141–148, <https://doi.org/10.1002/aenm.201100494>.
- [62] E.A.A. Aboelazm, G.A.M. Ali, H. Algarni, H. Yin, Y.L. Zhong, K.F. Chong, Magnetic electrodeposition of the hierarchical cobalt oxide nanostructure from spent lithium-ion batteries: its application as a supercapacitor electrode, J. Phys. Chem. C 122 (2018) 12200–12206, <https://doi.org/10.1021/acs.jpcc.8b03306.s001>.
- [63] J. Yan, C.E. Ren, K. Maleski, C.B. Hatter, B. Anasori, P. Urbankowski, A. Sarycheva, Y. Gogotsi, Flexible MXene/graphene films for ultrafast supercapacitors with outstanding volumetric capacitance, Adv. Funct. Mater. 27 (2017) 1701264, <https://doi.org/10.1002/adfm.201701264>.
- [64] A. Tomar, A. Joshi, S. Atri, G. Singh, R. Sharma, Zero-dimensional ordered Sr₂CoMoO_{6-δ} double perovskite as high-rate anion intercalation pseudocapacitance, ACS Appl. Mater. Interfaces 12 (2020) 15128–15137, <https://doi.org/10.1021/acsami.9b22766>.
- [65] C. Wang, S. Zhai, Z. Yuan, J. Chen, Z. Yu, Z. Pei, F. Liu, X. Li, L. Wei, Y. Chen, Drying graphene hydrogel fibers for capacitive energy storage, Carbon 164 (2020) 100–110, <https://doi.org/10.1016/j.carbon.2020.03.053>.
- [66] K.M. Hercule, Q. Wei, O.K. Asare, L. Qu, A.M. Khan, M. Yan, C. Du, W. Chen, L. Mai, Interconnected nanorods-nanoflakes Li₂Co₂(MoO₄)₃ framework structure with enhanced electrochemical properties for supercapacitors, Adv. Energy Mater. 5 (2015) 1–7, <https://doi.org/10.1002/aenm.201500060>.
- [67] M.R. Lukatskaya, O. Mashtalir, C.E. Ren, Y. Dall'Agnese, P. Rozier, P.L. Taberna, M. Naguib, P. Simon, M.W. Barsoum, Y. Gogotsi, Cation intercalation and high volumetric capacitance of two-dimensional titanium carbide, Science 341 (2013) 1502–1505, <https://doi.org/10.1126/science.1241488>.
- [68] Q. Chang, L. Li, H. Qiao, L. Sai, Y. Zhang, W. Shi, L. Huang, Enhanced electrolyte ion penetration in microdome-like graphene with high mass loading for high-performance flexible supercapacitors, ACS Appl. Energy Mater. 2 (2019) 6790–6799, <https://doi.org/10.1021/acsaelm.9b01240.s001>.
- [69] K.V. Sankar, Y. Seo, S.C. Lee, S. Liu, A. Kundu, C. Ray, S.C. Jun, Cobalt carbonate hydroxides as advanced battery-type materials for supercapacitors: Influence of morphology on performance, Electrochim. Acta 259 (2018) 1037–1044, <https://doi.org/10.1016/j.electacta.2017.11.009>.
- [70] K. Li, Y. Shao, H. Yan, Z. Lu, K.J. Griffith, J. Yan, G. Wang, H. Fan, J. Lu, W. Huang, B. Bao, X. Liu, C. Hou, Q. Zhang, Y. Li, J. Yu, H. Wang, Lattice-contraction triggered synchronous electrochromic actuator, Nat. Commun. 9 (2018), <https://doi.org/10.1038/s41467-018-07241-7>.
- [71] X. Wu, Z.B. Zhai, K.J. Huang, R.R. Ren, F. Wang, Boosting energy and power performance of aqueous energy storage by engineering ultra-fine metallic VSe₂ nanoparticles anchored reduced graphene oxide, J. Power Sources 448 (2020) 1–7, <https://doi.org/10.1016/j.jpowsour.2019.227399>.
- [72] G.A.M. Ali, E. Megiel, P. Ciecior, M.R. Thalji, J. Romański, H. Algarni, K. F. Chong, Ferrocene functionalized multi-walled carbon nanotubes as supercapacitor electrodes, J. Mol. Liq. 318 (2020) 114064, <https://doi.org/10.1016/j.molliq.2020.114064>.
- [73] C. An, Y. Yuan, B. Zhang, L. Tang, B. Xiao, Z. He, J. Zheng, J. Lu, Graphene wrapped FeSe₂ nano-microspheres with high pseudocapacitive contribution for enhanced Na-ion storage, Adv. Energy Mater. 9 (2019) 1–9, <https://doi.org/10.1002/aenm.201900356>.
- [74] J. Qin, H. Maleki, K. Sari, X. Wang, H. Yang, J. Zhang, X. Li, Controlled design of metal oxide-based (Mn²⁺/Nb⁵⁺) anodes for superior sodium-ion hybrid supercapacitors: synergistic mechanisms of hybrid ion storage, Nano Energy 71 (2020), 104594, <https://doi.org/10.1016/j.nanoen.2020.104594>.
- [75] H. Deng, C. Zhang, Y. Xie, T. Tumlin, L. Giri, S.P. Karna, J. Lin, Laser induced MoS₂/carbon hybrids for hydrogen evolution reaction catalysts, J. Mater. Chem. A 4 (2016) 6824–6830, <https://doi.org/10.1039/c5ta09322h>.
- [76] M. He, K. Fic, E. Frackowiak, P. Novák, E.J. Berg, Ageing phenomena in high-voltage aqueous supercapacitors investigated by in situ gas analysis, Energy Environ. Sci. 9 (2016) 623–633, <https://doi.org/10.1039/C5EE02875B>.
- [77] J. Menzel, E. Frackowiak, K. Fic, Electrochemical capacitor with water-based electrolyte operating at wide temperature range, J. Power Sources 414 (2019) 183–191, <https://doi.org/10.1016/j.jpowsour.2018.12.080>.
- [78] X. Huang, Z. Zhang, H. Li, H. Wang, T. Ma, In-situ growth of nanowire WO_{2.72} on carbon cloth as a binder-free electrode for flexible asymmetric supercapacitors with high performance, J. Energy Chem. 29 (2019) 58–64, <https://doi.org/10.1016/j.jechem.2018.01.024>.
- [79] S.-H. Ji, N.R. Chodankar, D.-H. Kim, Aqueous asymmetric supercapacitor based on RuO₂-WO₃ electrodes, Electrochim. Acta 325 (2019) 134879, <https://doi.org/10.1016/j.electacta.2019.134879>.
- [80] P.A. Shinde, V.C. Lokhande, A.M. Patil, T. Ji, C.D. Lokhande, Single-step hydrothermal synthesis of WO₃-MnO₂ composite as an active material for all-solid-state flexible asymmetric supercapacitor, Int. J. Hydrogen Energy 43 (5) (2018) 2869–2880, <https://doi.org/10.1016/j.ijhydene.2017.12.093>.
- [81] H. Wang, G. Ma, Y. Tong, Z. Yang, Biomass carbon/polyaniline composite and WO₃ nanowire-based asymmetric supercapacitor with superior performance, Ionics 24 (2018) 3123–3131, <https://doi.org/10.1007/s11581-017-2428-8>.
- [82] A.K. Nayak, A.K. Das, D. Pradhan, High performance solid-state asymmetric supercapacitor using green synthesized graphene-WO₃ nanowires nanocomposite, ACS Sustain. Chem. Eng. 5 (2017) 10128–10138, <https://doi.org/10.1021/acsuschemeng.7b02135>.
- [83] S. Yao, F. Qu, G. Wang, X. Wu, Facile hydrothermal synthesis of WO₃ nanorods for photocatalysts and supercapacitors, J. Alloy. Compd. 724 (2017) 695–702, <https://doi.org/10.1016/j.jallcom.2017.07.123>.
- [84] S. Bobby, T. Kshetri, T. Ibomcha, N. Hoon, Embedded PEDOT : PSS / AgNFs network flexible transparent electrode for solid-state supercapacitor, Chem. Eng. J. 359 (2019) 197–207, <https://doi.org/10.1016/j.cej.2018.11.160>.
- [85] T. Purkait, G. Singh, D. Kumar, M. Singh, R.S. Dey, High-performance flexible supercapacitors based on electrochemically tailored three-dimensional reduced graphene oxide networks, Sci. Rep. 8 (2018) 1–13, <https://doi.org/10.1038/s41598-017-18593-3>.
- [86] K.D. Fong, T. Wang, H.-K. Kim, R.V. Kumar, S.K. Smoukov, Semi-interpenetrating polymer networks for enhanced supercapacitor electrodes, ACS Energy Lett. 2 (2017) 2014–2020, <https://doi.org/10.1021/acsenergylett.7b00466.s001>.
- [87] S.A. Pawar, D. Kim, R. Lee, S. Kang, D.S. Patil, T. Wan, J. Cheol, Efficient supercapacitor based on polymorphic structure of 1T'-Mo₆Te₆ nanoplates and few-atomic-layered 2H-MoTe₂: a layer by layer study on nickel foam, Chem. Eng. J. 371 (2019) 182–192, <https://doi.org/10.1016/j.cej.2019.04.009>.